Chapter 6
When Diffraction Stops and Destruction Begins

Carl Caleman and Andrew V. Martin

6.1 Introduction

It is now possible to solve protein structures with femtosecond X-ray free-electron laser (XFEL) pulses that were previously inaccessible to continuous synchrotron sources due to radiation damage [1, 2]. The key to this success is that diffraction probes the protein structure on femtosecond timescales, whereas nuclear motion takes tens to hundreds of femtoseconds to have a significant effect on the crystal structure. This is the essential idea behind the diffraction-before-destruction principle that underlies serial femtosecond crystallography (SFX) with XFELs [1]. In practice, the principle works well enough to determine protein structures of comparable resolution to synchrotron protein crystallography [2], which has led to the many successes of XFEL crystallography to date.

The reality is, however, that radiation damage begins from the first femtosecond that the pulse interacts with the sample and begins to affect diffraction through electron motion. The signal adds incoherently during the exposure and the measured pattern is the accumulated diffraction from an initially undamaged crystal as it gradually degrades and becomes disordered [3]. A striking feature of crystal samples is that the induced motion changes the nature of the diffraction during the pulse

---

C. Caleman (✉)
Department of Physics and Astronomy, Uppsala University, Uppsala, Sweden

Center for Free-Electron Laser Science, Deutsches Elektronen-Synchrotron, Hamburg, Germany
e-mail: carl.caleman@physics.uu.se

A. V. Martin
School of Science, RMIT University, Melbourne, VIC, Australia

ARC Centre of Excellence for Advanced Molecular Imaging, University of Melbourne,
Melbourne, VIC, Australia
e-mail: andrew.martin@rmit.edu.au

S. Boutet et al. (eds.), *X-ray Free Electron Lasers*,
https://doi.org/10.1007/978-3-030-00551-1_6

from sharp Bragg peaks to continuous diffuse scattering. The crystalline Bragg diffraction may stop completely before the end of the pulse, but the measured pattern will still contain Bragg peaks so long as they are larger than the background noise generated by the diffuse scattering integrated over the whole pulse duration. This has been dubbed the "self-gating" effect [3], as crystal diffraction appears to have been generated by shorter pulse of the same intensity. The self-gating effect is resolution dependent as Bragg diffraction will only stop at a particular scattering angle when the damage has spread to the corresponding length-scale in the sample.

Damage processes that affect all atoms approximately equally independent of atom species or position within the sample are commonly referred to as "global damage". These processes include the average ionization level throughout the sample and ion motion due to the rising average temperature during the exposure. The effect of global damage on the diffraction can be modelled as an attenuation factor that varies with scattering angle (i.e. resolution). This is a similar effect to the temperature factors used in synchrotron crystallography, except the dependence on scattering angle can be different (non-Gaussian) in the XFEL case and sensitive to experimental conditions. We will review the physical origins of the attenuation of diffraction by global damage in this chapter.

Local damage is any damage process that does not affect all atoms in the sample equally, i.e. is element specific, depends on local environment or depends on the position of an atom. The effect most likely to be encountered is a relative change in the scattering strength of different elements caused by differences in ionization rates. This is expected when heavy elements are present and there are large differences in atomic number between elements in the sample [4, 5]. In some cases, this is an advantage because it can increase multiple anomalous absorption signal that can be used for ab initio phasing [6]. Variable ionization rates between elements also have subtler effects on the coherence of the diffracted X-rays [7].

While most of the damage effects encountered in XFEL protein crystallography are captured by the concepts of global and local damage, there have also been observations of exotic, cooperative structural changes in inorganic crystals. These are dynamical changes in highly ionized crystals on femtosecond timescales that modify the observed crystal structure. A striking example of electron dynamics is the cooperative motion that was observed in C_{60} fullerene crystals [8], effectively changing crystal structure as seen by the X-rays. It has also been shown using a two-colour X-ray pump-probe experiment on crystalline xenon clusters that when widespread ionization drives the sample into a plasma-like state, the lattice spacing of a crystal can contract on sub-100 fs timescales [9]. While these exotic, cooperative effects have not been observed in protein crystals, and may even be unlikely, they do serve as a warning that nothing can be taken for granted in XFEL experiments.

In synchrotron crystallography, a key measure of damage tolerance in crystals is dose, which is the absorbed energy in the sample per unit mass. For cryocooled macromolecules, an estimated limit is 30 MGy [10]. In these terms, XFELs massively exceed this limit by solving protein structures with doses of tens of giga-Gray [11]. However, for the femtosecond timescale of XFEL pulses, dose is not the best predictor of radiation damage effects. Induced sample dynamics are more sensitive to the rate at which energy is absorbed, which could be expressed as a dose rate, but more commonly is quantified by the incident beam intensity, which facilitates the specification of experimental parameters.

While the concept of diffraction-before-destruction serves as a good working principle to understand why XFEL crystallography works, there is a complex competition between damage and diffraction that ultimately determines suitable beam conditions for XFEL crystallography. Our aim in this chapter is to review the background theory of damage and diffraction in XFEL crystallography and to discuss what is known about radiation damage from XFEL crystallography experiments so far.

6.2 Damage Processes and Modelling

6.2.1 Ionization Processes

X-rays interact with matter through scattering and absorption. Photon scattering can either be elastic, where the photon energy is conserved, or inelastic, where some of the photon energy is transferred to the atom. Generally, elastic scattering contributes to the recordable information in the diffraction pattern, while inelastic scattering does not carry structural information that is easily decipherable. In photoabsorption, the energy of the photon is transferred to an electron, which is then ejected from the atom, leaving a positively charged ion behind. Figure 6.1 shows the cross section

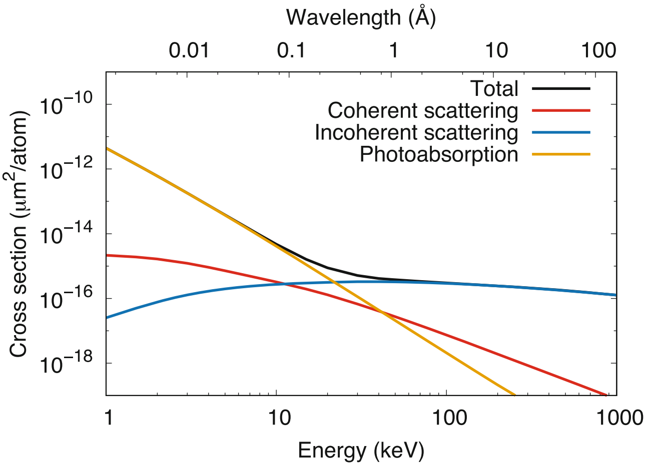

Fig. 6.1 Cross sections vs energy. Atomic cross sections of neutral carbon for photoabsorption, coherent scattering and incoherent (Compton) scattering

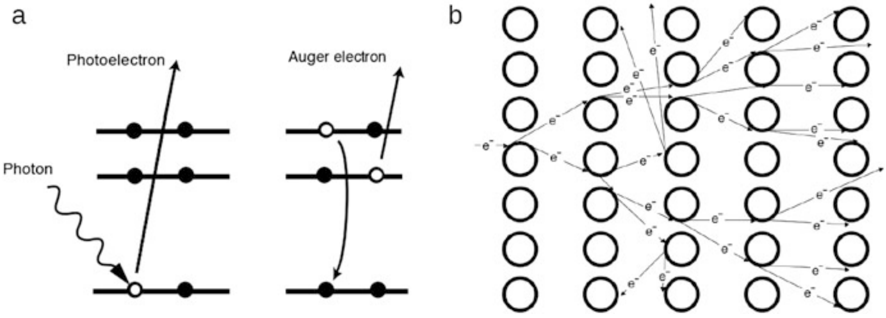

Fig. 6.2 Ionization processes. Diagrams illustrating the processes of (**a**) photoabsorption and Auger decay, and (**b**) the secondary electron cascade. The crystal approaches a plasma-like state as secondary ionization becomes widespread. Reproduced with permission from Caleman [18]

for the photon interaction with carbon at energies relevant for SFX. At 10 keV the probability for photoabsorption is around ten times higher than that for coherent scattering. Hence, this is the main process that leads to damage in the sample.

When the photoelectron ejected from a core level leaves behind a vacancy, an electron from a higher energy level may fall into the empty orbit, resulting in a release of energy. This energy may be emitted in the form of a photon (dominant process with high-Z elements), but it can also be transferred to an outer shell electron, which is then ejected from the atom in a process called Auger decay [12] as illustrated in Fig. 6.2a. The Auger electron carries the kinetic energy corresponding to the difference between the shell binding energy and the energy of the initial electronic transition. Compared to the photoelectron generated by an X-ray photon, the energy of the Auger electron is significantly lower, and it is ejected at a later time than the photoelectron. In biologically relevant material Auger electrons have energies between 250 eV and 2 keV [13], compared to the photoelectron carrying the energy of the incoming photon minus the shell binding energy (typically between 2 and 20 keV with X-rays). The physics of this decay is well understood [14]. The lifetime of the inner level vacancy caused by photoionization can be determined by measurements of the Auger line widths [15]. For atoms abundant in biological samples (such as C, N, O and S), the K-hole lifetimes are up to around 10 fs. During the photoionization process, the photoelectron may interact with valence electrons, leading to the so-called shake-up and shake-off effects [16]. For light elements of biological significance, electron emission from these effects is on the order of 10–30% of the events where a low energy electron (10–100 eV) is emitted [17].

Inelastic scattering is a relatively rare event at X-ray frequencies although it is the main source of energy deposition with hydrogen, and represents about 3% of all interactions between X-rays and a biological sample at 1 Å wavelength. During inelastic scattering, the incoming photon excites an electron to some virtual level and when the electron relaxes emitting a photon, it does not come back to the ground state. The photon emitted has therefore a different frequency from the photon absorbed, and it also has an altered phase.

As atoms are photo-ionized, the electrons ejected from the atom will interact with the surrounding sample. In a macroscopic sample, both the photoelectrons and the secondary Auger electrons become thermalized and trapped inside the sample. Thermalization is based on inelastic electron–electron interactions and, to a lesser degree, on electron–nuclear interactions. An electron scattering inelastically on an atom may cause a second ionization of an outer shell electron. This mechanism leads to an avalanche of electrons generated from one single photoionization event as shown in Fig. 6.2b. Thermalization produces a large number of such secondary ionization events, known as electron cascades or electron avalanche [19]. The number of these cascade electrons is roughly proportional to the energy of the impact electron triggering the cascade. These electrons are redistributed in the sample and can recombine with atoms. On the 100 fs timescale, considered relevant to damage formation in structural biology with XFELs, the recombination is low [20].

Collisions with atoms are highly relevant for understanding of X-ray induced damage. In a near neutral organic sample, where most atoms have their outer shell electrons bound, a single Auger electron from a carbon atom, carrying a kinetic energy of 278 eV, will generate up to 12 secondary electrons [21]. An 8 keV photon electron, on the other hand, might in the same sample cause up to 400 secondary ionization events, as illustrated in Fig. 6.3. The thermalization happens within tens of femtosecond, which means that 10–30 fs after a single photo-ionization event, more than 400 secondary ionization events have occurred in the sample [11].

The description above is valid for a neutral system, where most atoms carry all their electrons. In an SFX experiment, the photon bombardment is so intense

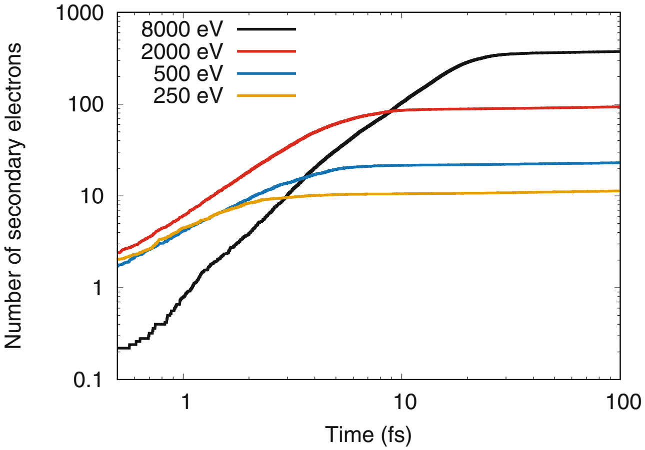

Fig. 6.3 Electron cascades at different energies. The cascade of electrons generated by a single electron of energy 250, 500, 2000 and 8000 eV in an neutral organic crystal, urea. The calculations were performed using a molecular dynamics code, as in Caleman et al. [22]. The number of secondary electrons generated is plotted as a function of time after the photon absorption event

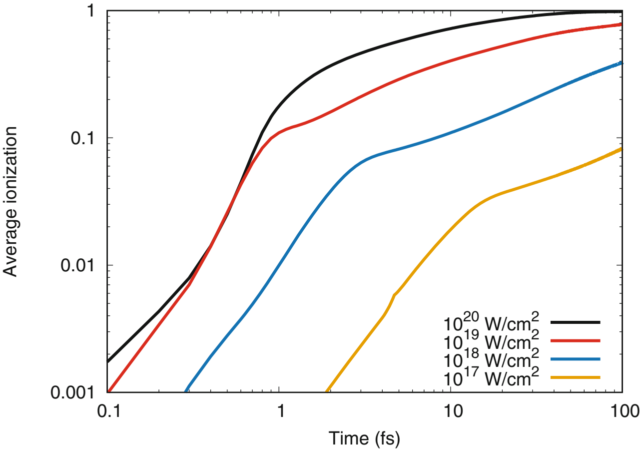

Fig. 6.4 Average ionization in a sample vs time for different intensities. Average ionization in a photosystem I protein crystal exposed to a 100 fs XFEL pulse with different pulse intensities. Photon energy was 6 keV and the simulations are performed using a continuum model [24, 25]. When the average ionization becomes constant in time, all the electrons are stripped from the atoms and the atoms become transparent to the X-rays

that the average ionization in a sample often rises well above one per carbon atom. This affects both the photoionization probability and the electron impact ionization. Photoionization at the relevant X-ray energies acts on the core s-electrons. If the vacancies caused by photoionization cannot be refilled by outer shell electrons, the sample in principle becomes transparent to the X-ray photons and cannot absorb more energy through photoionization. This has been described in early experiments at the linac coherent light source (LCLS) using Neon atoms as a target [23], but is equally relevant for biological samples. The electron–electron ionization probability is altered in a similar way. At high average ionization states the number of valence electrons is reduced and, hence, so is the inelastic free-electron valence–electron interaction. In Fig. 6.4 the average ionization of all atoms in a photosystem I protein crystal is shown and predicted by simulations using a continuum model [26], described below.

6.2.2 Ion Motion

The ionization caused by the X-ray bombardment causes the sample to heat up. The ions are put into motion due to the electron–ion collisions, ion–ion collisions and local electric fields. As the sample is heated up and ionized, it can be physically described as a plasma. In this description the ion diffusion coefficient D_i can be theoretically calculated, based on the ion temperature and the ion collision frequency ν_i [27]:

$$D_i(t) = \frac{k_\mathrm{B} T_i(t)}{m_i \nu_i(t)} \,, \tag{6.1}$$

where m_i is the mass and k_B is the Boltzmann constant. This model assumes that each element i can be assigned a time-dependent temperature $T_i(t)$. The ion temperatures can be predicted using a quantum kinetic approach from warm dense plasma theory [28] using information about the trapped electrons that effectively heat the ions. From the ion diffusion coefficient it is further possible to calculate the root mean square displacement (RMSD) of the ions as

$$\sigma(t) = \sqrt{2N D_i(t) t} \,, \tag{6.2}$$

where N is the number of dimensions. The shape of the RMSD as a function of time is not strongly dependent on the intensity and could be represented by a scaling law;

$$\sigma(t) = B t^n \,, \tag{6.3}$$

with $n \sim 1.5 \pm 0.4$ [25] and B is a fitting parameter that can be estimated from simulation. Figure 6.5 shows the RMSD for some examples relevant to SFX, estimated using the scaling law.

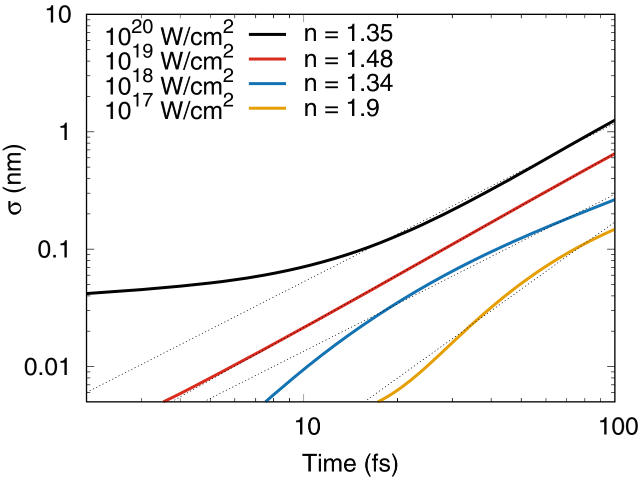

Fig. 6.5 Calculated ion displacement in a sample vs time at different intensities. Root mean squared displacement (σ) of the carbon ions in a photosystem I crystal exposed to a 100 fs XFEL pulse with photon energy of 6 keV, as simulated in Caleman et al. [25]. The dotted lines are the best fit using the scaling law described in the main text, with the B and n parameters estimated from continuum simulations

6.3 Damage Modelling

The potential in biological imaging using XFEL pulses was pointed out in a study by Neutze et al. [29] in the year 2000, well before any XFEL sources were available. In the following years several studies focusing on the optimal pulse parameters were published [30–32], all of them pointing out that the X-ray pulses needed to be shorter than the timescales of the destruction of the molecular structure of the sample. These studies and early experiments at the test facility at Stanford, SPPS [33, 34], were important to pave the way towards the investments and scientific efforts that lead to the building of the XFEL facilities we have today. The simulations, in particular the scientific case presented in Neutze et al. [29], were one of the major factors that made the scientific community realize the potential in biological imaging with an XFEL.

Simulations have been a natural part of the development of SFX. Early on they were used to explore the potential of using XFEL sources for structural biology, then later they informed the design of end stations and have been used to interpret the effects of radiation damage on experimental diffraction data. For large organic samples such as biomacromolecules and protein crystals, two major modelling approaches have been used. The study by Neutze et al. [29] applied a molecular dynamics (MD) approach. They used a well-established MD code that was adopted to include ionization and bond breaking. The models describing the physics in this early study were simplistic, but nevertheless the major conclusions drawn in the study still hold.

Since then several studies have used the MD approach and developed the model used in the early simulation. It is worth mentioning the so-called Cimarron Project [35], developed at Lawrence Livermore National Laboratory. The code is developed to simulate dense plasmas and has been applied to biological samples [36]. Another MD initiative developed to study FEL-matter interaction is the Xraypac [37] suite of programs that include both a MD part, XMDYN, and atomic ionization part, XATOM [38], that is based on nonrelativistic quantum electrodynamics and perturbation theory within the Hartree-Fock-Slater model. In general, molecular dynamics codes are rather computationally expensive to use, especially for large systems such as protein crystals. This necessitates the use of simplified descriptions of complex physical processes, such as bond breaking and ionization. However, MD codes have the advantage of giving direct information of the positions of the nuclei. Knowledge about the nuclei positions together with the ionization levels means that, in theory, the expected diffracted signal can be calculated directly from the simulations.

The second major approach to simulate the photon–matter interaction in an XFEL experiment has been by using rate equations to keep track of radiation transfer, ionization and temperatures. This description does not consider the time evolution of individual atoms, but rather describes a material as a continuum with specific properties. These models are often referred to as continuum models and are highly similar to models applied in other fields of research, like plasma and warm dense matter physics. A continuum model was first used for the purpose of understanding the dynamics in biological samples exposed to an FEL by Hau-Riege et al. in 2004 [30]. Since then this approach has been applied several times. Codes originally developed for warm dense matter physics applications, the so-called non-local thermal equilibrium codes (NLTE), have been used in several studies to describe the damage processes in SFX [3, 11, 25, 39]. The continuum model approach has the advantage over the MD approach that it is much less computationally expensive and does not scale with particle size. However, since everything is treated as ensembles it does not give any information about the individual atoms or ions. Any estimate of atomic displacement (and, in turn, decrease in diffracted signal) has to be calculated based on average ion temperatures. Changes in the diffracted signal caused by collective motion or local damage are not captured by this model, whereas such effects would be described, in principle, in a simulation considering the dynamics of the individual particles.

6.4 Diffraction and Damage

6.4.1 XFEL Diffraction Theory

X-rays are scattered by the electrons in the sample and the theory of XFEL crystal diffraction starts with a dynamical electron density for the sample, $\rho(q,t)$, and its Fourier transform, $f(q,t)$, called the atomic scatter factor. Diffraction at large scattering angles encodes high resolution structural information and is primarily caused by electrons that are still bound to atoms. The electrons that are ejected in ionization processes are delocalized and scatter X-rays diffusely to lower scattering angles, which is less important for crystallography experiments but contributes to the overall background.

There are two main impacts of XFEL damage on crystal diffraction: (1) the depletion of bound electrons and (2) the motion of ions due to Coulomb repulsion or diffusion. Both the depletion of bound electrons and ion motion break the translational symmetry of the crystal. This changes the nature of the diffraction from discrete to diffuse scattering. Hence, the characteristic effect of damage on the diffraction pattern is the decrease in Bragg diffraction relative to the diffuse background.

Due to the weak interaction between X-rays and matter, the X-ray diffraction pattern from a crystal can be expressed in terms of the crystal's time-dependent scattering factor $F(\mathbf{q},t)$. The diffracted intensity $I(\mathbf{q})$ through a small solid angle $\Delta\Omega$ centred at scattering vector $\mathbf{q}$ is given by

$$I(\mathbf{q}) = r_e^2 \Delta\Omega \int I_0(t) |F(\mathbf{q},t)|^2 dt \ , \tag{6.4}$$

where r_e is the classical electron radius, $I_0(t)$ is the incident intensity and t is time. For the simulation of an experiment, the intensity distribution measured on a detector can be estimated by setting $\Delta\Omega$ equal to the solid angle spanned by each pixel. The vector $\mathbf{q}$ indicates the point in reciprocal space that intersects the Ewald sphere. The crystal scattering factor is assumed to be a sum of the atomic scattering factors $f_i(\mathbf{q}, t)$ multiplied by a phase term that specifies the position of each atom in the crystal:

$$F(\mathbf{q}, t) = \sum_i f_i(\mathbf{q}, t) e^{-2\pi i \mathbf{q} \cdot \mathbf{r}_i(t)} , \tag{6.5}$$

where i ranges over the number of atoms in the crystal. The decomposition of the crystal scattering factor into a sum of atomic scattering factors is known as the isolated atom approximation, because it ignores bonding between atoms. The diffraction is impacted by ion diffusion through the time-dependence of the ion position $\mathbf{r}(t)$. The atomic scattering factors are parameterized into a $\mathbf{q}$-dependent factor $f_i^{(0)}(\mathbf{q})$ that depends on the electron density and wavelength dependent correction factors (f_i' and f_i''):

$$f_i(\mathbf{q}, t) = f_i^{(0)}(\mathbf{q}, t) + f_i' + i f_i'' . \tag{6.6}$$

The first term on the right-hand side, $f_i^{(0)}(\mathbf{q}, t)$, is proportional to Fourier transform of the atom's electron density $\rho(\mathbf{q}, t)$ and is thus sensitive to the number of electrons around an atom. Figure 6.6 shows how the scattering factor changes with ionization state for carbon. An important detail to note is that core-shell

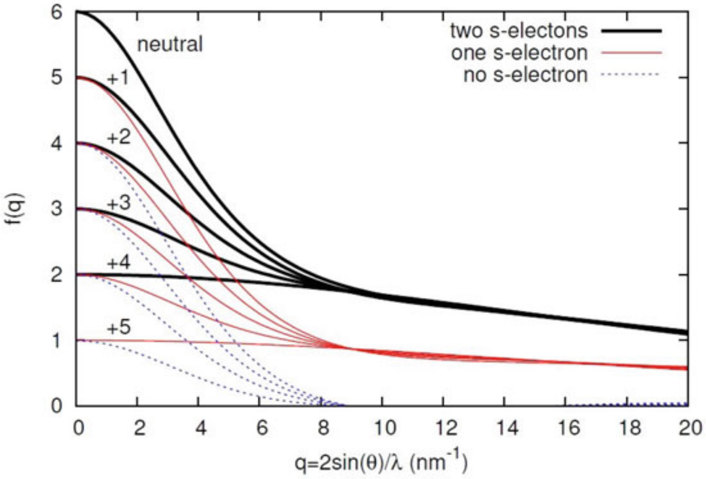

Fig. 6.6 Ionic scattering factors. The ionic scattering factors for carbon in different ionization states. Reproduced with permission from Caleman et al. [25]

electrons are almost the sole cause of scattering at resolutions greater than 3 Å. Hence, core-shell ionization and valence-shell ionization do not have equivalent effects on the diffraction pattern. As described in Sect. 6.2.1, core-shell and valence-shell ionization are also caused by different damage mechanisms. Valence-shell ionization, in particular, is more prevalent at later times during the exposure when the crystal is driven into a plasma-like state.

6.4.2 The Effect of Ionization on Crystal Diffraction

The difference between diffraction in synchrotron and XFEL crystallography is due to the extent to which scattering factors $f_i^{(0)}(\mathbf{q}, t)$ fluctuate during an exposure due to the widespread ionization. The effect of ionization is to reduce the number of bound electrons around an atom, which reduces the scattering strength $f_i^{(0)}(\mathbf{q}, t)$. This reduction of bound electrons occurs stochastically, which can have a significant effect on the diffracted intensities. For neutral atoms, scattering can be taken from parameterized tables [40]. For ionic scattering factors, the electron density is reconstructed from the densities of the remaining bound electrons. The densities of individual electron densities can be approximated with Slater orbitals [41]. Alternatively they can be calculated with quantum mechanically with code specifically designed for XFEL research, such as XATOM [38].

Both photoionization and secondary ionization are assumed to be random and not correlated between different unit cells or different atoms. The diffraction from atoms in different unit cells that are equivalent by lattice translation adds constructively at the Bragg condition. In the case of electronic damage, this effectively averages the scattering factor of an atom over the distribution of ionization states. Hence, the scattering factor for the crystal can be modelled by replacing each atomic scattering factor $f_i(\mathbf{q}, t)$ by its average over ionization states $\langle f_i(\mathbf{q}, t)\rangle$, as follows:

$$\langle F(\mathbf{q}, t)\rangle = \sum_i \langle f_i(\mathbf{q}, t)\rangle e^{-2\pi i \mathbf{q}\cdot\mathbf{r}_i(t)} . \tag{6.7}$$

Ignoring effects of the local structural environment on ionization leads to all atoms of the same species being modelled by the same average scattering factor. As a first approximation to model the global effects of damage, the diffracted intensity can be further averaged over different elements, which leads to the following approximation:

$$\langle |F(\mathbf{q}, t)|^2\rangle \approx \frac{\langle f^2(q, t)\rangle}{f_0^2(q, t)} |F(\mathbf{q}, t)|^2 + Nx(1 - x)\Delta f^2(t) , \tag{6.8}$$

where x is the fraction of atoms that have been ionized and N is the total number of atoms. The first term on the right-hand side of Eq. (6.8) is proportional to the undamaged scattering factor squared and represents coherent scattering, while the second term is the incoherent continuous background. We denote the global ionization scaling factor by

$$k(q,t) = \langle f^2(q,t)\rangle / f_0^2(q,t)\ . \tag{6.9}$$

We refer to this effect as global because it models the average ionization over all atoms. It has the same effect on each atom independent of element and atomic position.

Different elements will ionize at different rates and heavy elements have more electrons to lose than lighter elements. The change of relative strength of the different elements is a type of local damage that cannot be accounted for by an overall scaling of the diffraction. The difficulty with local damage is that it has the potential to change the interpretation of the structure. The bulk of atoms in protein crystals are light elements C,O and N, which will ionize at similar rates, and the effect of variable ionization is more likely to be observed in heavier elements relative to lighter elements. It is thus an important factor for methods of structure determination that explicitly use the scattering of heavy ions, such as anomalous dispersion or isomorphous replacement. It has even been proposed that in XFEL crystallography, higher ionization rates can increase the anomalous signal and be favourable [6].

6.4.3 The Effect of Ion Motion on Diffraction

To account for the effect of ion motion, the position of the ion can be written as a sum of its initial position plus a time-dependent displacement

$$\mathbf{r}_i(t) = \mathbf{R}_i + \boldsymbol{\epsilon}_i(t)\ . \tag{6.10}$$

Models of ion diffusion and temperature effects assume that $\boldsymbol{\epsilon}_i(t)$ is a random displacement with the statistics of a random walk. When the structure factor is averaged with respect to these statistics (and ionization is ignored) it takes the form

$$\langle |F(\mathbf{q},t)|^2\rangle = |F_0(\mathbf{q},t)|^2 e^{-4\pi^2 q^2 \sigma^2(t)}\ , \tag{6.11}$$

where

$$F_0(\mathbf{q},t) = \sum_i f(\mathbf{q}) e^{-2\pi i \mathbf{q}\cdot\mathbf{R}_i}\ . \tag{6.12}$$

The form of Eq. (6.11) is the same as the usual temperature factor in crystallography, except that the width is time-dependent to account for the effective change in temperature described in Sect. 6.2.2.

Ignoring ionization, the global correction factor for ion motion is constructed by integrating the time-dependent temperature factor:

$$g(q;T) = \int_0^T I_0(t) \exp^{-4\pi^2 q^2 \sigma^2(t)} \, dt \; . \tag{6.13}$$

The new expression for the diffracted intensity with the global correction for ion motion is

$$I(\mathbf{q}) = r_e^2 \Delta\Omega g(q;T) |F_0(\mathbf{q},t)|^2 \; . \tag{6.14}$$

The effect of time-dependent ion diffusion on the diffraction is illustrated in Fig. 6.7. The crystal is initially highly ordered and produces Bragg diffraction. By 35 fs, ion motion has disrupted most of the high resolution structure of the crystal, leaving only periodicity at lower resolution, and by 70 fs all periodic structure is

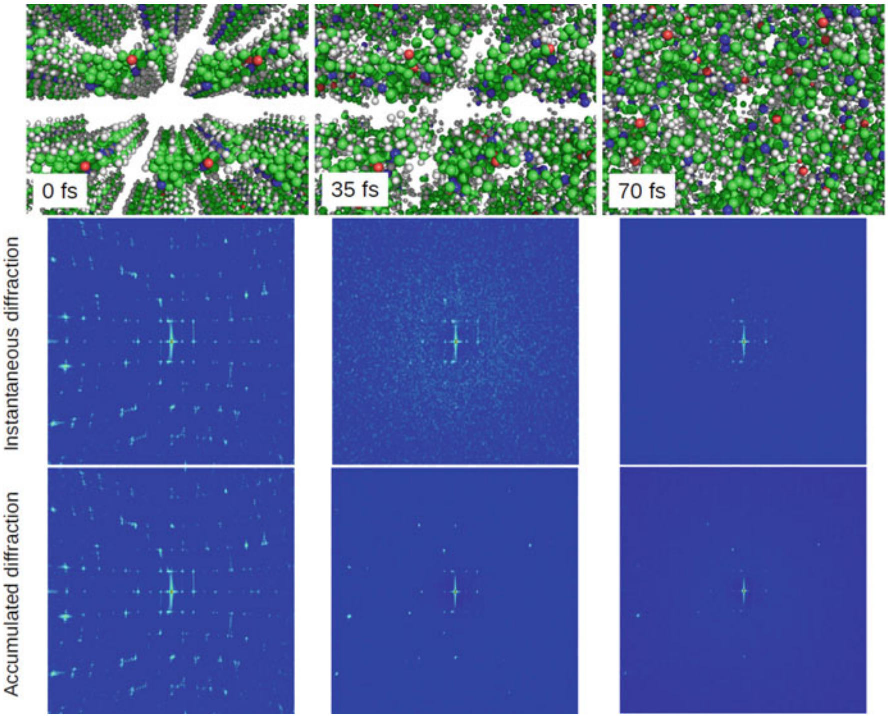

Fig. 6.7 The effect of ion diffusion on crystal diffraction. The top row shows the ion positions of a lysergic acid diethylamide crystal at different times during the exposure. The middle row shows the instantaneous diffraction pattern from each structure, which is the contribution to the measured intensity from that moment in time. The bottom row shows the accumulated diffraction which corresponds to the measured intensity

gone. This is reflected in the instantaneous diffraction patterns, which show only low resolution Bragg peaks at 35 fs and no Bragg peaks at 70 fs. However, the measured intensity is accumulated as the pulse traverses the sample and still shows Bragg peaks at 70 fs, because these were generated at earlier pulse times. Most importantly the Bragg peaks have greater magnitude than the noise generated by the increased diffuse background. Figure 6.8a shows how the accumulation of the Bragg signal stops at different moments during the pulse according to resolution. This leads to a relative resolution-dependent scaling of the Bragg peaks given by $g(q, T)$, which is plotted for different pulse times in Fig. 6.8b.

6.4.4 Global Correction Combining Ionization and Ion Motion

Combining the global corrections for ionization, Eq. (6.8), and for ion motion Eq. (6.11), we obtain a new expression for the diffracted intensity:

$$I(\mathbf{q}) = r_e^2 \Delta\Omega |F(\mathbf{q}, t)|^2 \int I_0(t) k(q, t) e^{-4\pi^2 q^2 \sigma^2(t)} dt \ . \tag{6.15}$$

The time integral on the right-hand side of Eq. (6.15) represents the global correction factor for both ion motion and ionization. As shown in Fig. 6.6, core-shell electrons make up a greater fraction of the scattering factor at high resolution. Hence, core-shell ionization is expected to reduce high resolution peaks relative to low resolution peaks, adding to the initial effects of ion motion. Interestingly, valence-shell ionization can have the opposite effect. Figure 6.6 shows that valence electrons contribute to the scattering factor at resolutions up to 3 Å and when valence ionization dominates low resolution peaks can be attenuated relative to high resolution peaks. This effect is predicted by the simulations shown in Fig. 6.9. At lower intensities ($10^{17} - 10^{18}$ W cm^{-2}) ion motion and core-shell ionization dominate and high resolution peaks are most affected, but at higher intensities ($10^{19} - 10^{20}$ W cm^{-2}) valence ionization dominates global damage and the low resolution peaks are more greatly affected.

6.4.5 Partial Coherence Effects in XFEL Crystallography

In addition to modifying the crystal scattering factor, XFEL radiation damage can also change the coherence properties of the diffracted X-rays. This effect has been predicted for single molecule studies [42], but was largely assumed to be absent for crystal diffraction. Although each unit cell is damaged differently within a single exposure, the scattered waves from all the units cells interfere constructively at the Bragg condition, motivating the assumption that diffraction can be modelled from the average crystal electron density. However, the time integral in Eq. (6.4)

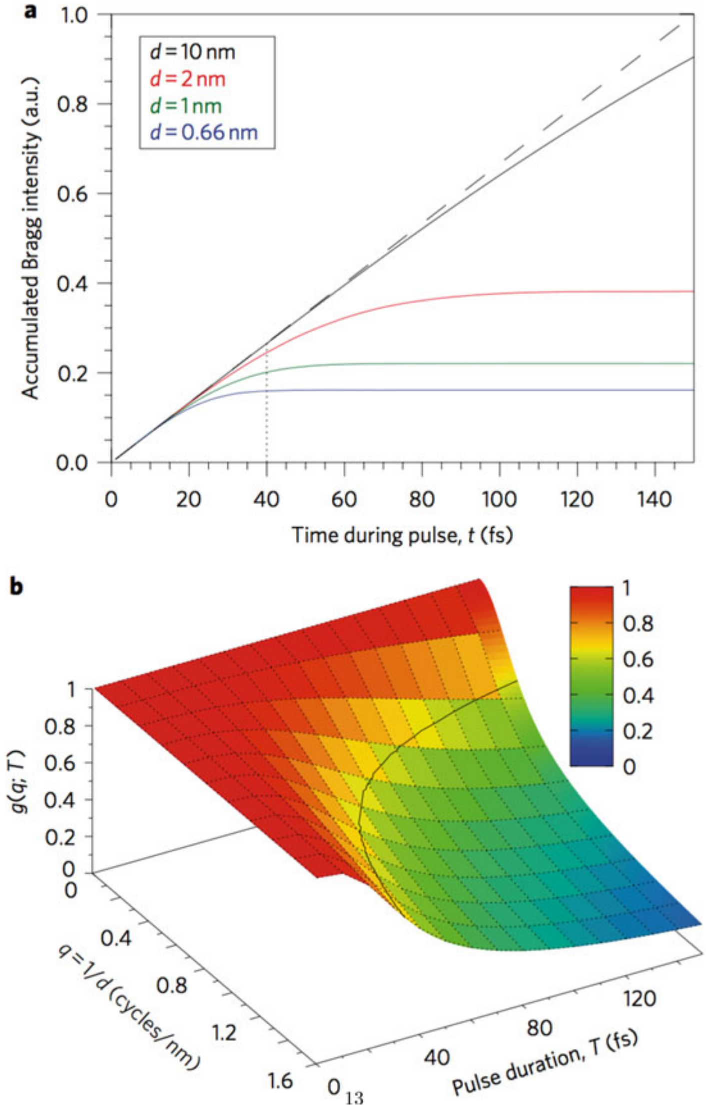

Fig. 6.8 Attenuation function due to ion motion. (**a**) The accumulation of the Bragg peak intensity at different resolutions as a function of the interaction time with the pulse predicted by the code CRETIN for a homogeneous protein sample in water. (**b**) The attenuation function due to ion motion as a function of pulse duration and resolution. Adapted from Ref. [3]

means that this is not entirely true. Fortunately, a more detailed analysis finds that for crystals, a full-coherence (single mode) approximation is valid, albeit with a slightly modified interpretation of the scattered wave [7]. With coherence effects included, the contribution of an ion to the scattered beam will not necessarily be

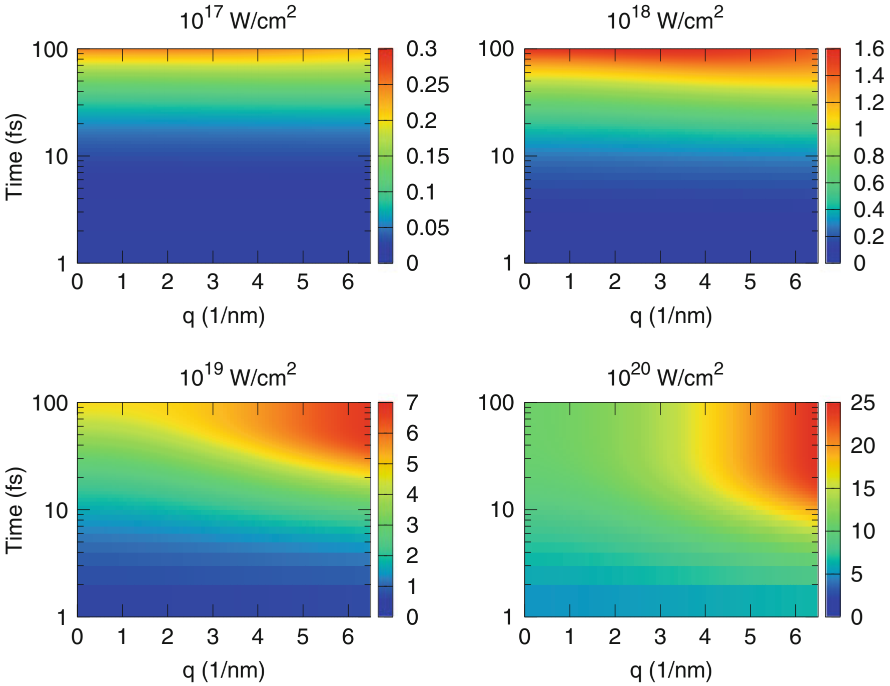

Fig. 6.9 Attenuation function due to ion motion and ionization. The attenuation function due to both ion motion and ionization as a function of pulse duration and resolution for different incident beam intensities. The relative attenuation of low and high angle scattering changes as intensities increase from low values (10^{17} W/cm^2–10^{18} W/cm^2) where diffusion dominates to higher values (10^{19} W/cm^2–10^{20} W/cm^2) where ionization effects dominate. The value for 6 keV and 10^{17} W/cm^2 is normalized to 1 to facilitate comparison with the different cases. Only ionization and displacement of carbon atoms are shown. Reproduced with permission from Caleman et al. [25]

equal to time-averaged scattering factor for each atom. This is only likely to affect crystals that have heavy elements and exposed to very high beam intensities, e.g. an effect of up to 20 % is predicted for sulphur exposed to high beam intensities.

6.5 SFX Damage Experiments

The first two experiments [3, 43] to study damage in SFX were performed at 2 keV at LCLS and spanned pulse durations from 70 to 400 fs. By studying long pulse durations, extensive radiation damage occurred and unique aspects of XFEL radiation damage were observed for the first time in serial crystallography samples. In particular, the experiment on photosystem I crystals [3] probed a region where ion motion effects dominated the global damage. This enabled the validation of a time-dependent temperature factor given in Sect. 6.4.3, as reasonably good agreement was achieved between the experimental data and modelling with CRETIN. This established the principle of damage effectively gating the pulse, so that the pulse appeared apparently shorter in duration. Excitingly, it gave explanation for why Bragg peaks were observed in SFX experiments even when the damage processes were expected to destroy the crystalline order before the end of the pulse. It is the diffraction from the early part of the pulse that generates the Bragg peaks, while the latter parts of the pulse produce a greater proportion of diffuse scattering. The experiment on lysozyme [43] under very similar experimental conditions was analysed with conventional time-independent temperature factor analysis and found inconsistencies between datasets at different pulse lengths, and between the XFEL data and synchrotron data of the same sample. The lack of agreement between datasets was not correctable with a global (time-dependent) factor for ion motion, leaving open the increased impact of global or local ionization effects on this sample.

The photosystem and lysozyme experiments formed part of the early development of SFX prior to the availability of shorter wavelength instruments. It was a positive development for SFX that hard X-ray pulses with photon energy 8–10 keV produce less radiation damage than the early experiments at 2 keV. Using crystals close to one micron in size with a comparable beam size, the intensity is sufficiently low to enable standard crystallographic analysis, without further modification for global or local XFEL damage. This was first confirmed in an experiment on lysozyme [2] and was soon confirmed with studies of other protein crystals. Structures had resolutions in the range of 2–3 Å sufficient for fitting atomic models. The validity of conventional analysis for a useful range of XFEL beam conditions has underpinned the rapid rise of this technique to date.

There are many SFX experiments that require higher intensities or smaller beam sizes for which radiation damage is critically important. In particular, recent efforts have focused on the potential for local damage in heavier ions such as sulphur or iron, as these elements are of biological importance and are also important for phasing based on anomalous scattering or isomorphous replacement. An important development for the SFX community was the demonstration of ab initio phasing by anomalous scattering of lysozyme soaked in an organometallic gadolinium complex [44], which showed that SFX data from an XFEL was of sufficient quality for this technique. This implies also that the extensive ionization does not eliminate heavy atom signal on which this technique is based. The extent of the ionization of gadolinium atoms in lysozyme was studied as a function for two different fluences (high and low) [45], and an average difference of almost nine electrons per Gd atom was found. The ionization was significantly lower than predicted by the XATOM code [38], and the possible explanations given included electron transport, recombination, ion motion or the unknown beam intensity profile.

Single anomalous dispersion has been demonstrated with sulphur [46, 47] and selenium [48] using XFELs, which is highly positive development for de novo phasing because sulphur and selenium are widely used for de novo phasing in synchrotron crystallography. This followed an earlier study of ionization in sulphur that reported an increase in the anomalous signal for XFEL sources compared to synchrotron sources [4].

An experiment designed to specifically target local damage effects was conducted on ferredoxin crystals with a beam intensity approaching the highest available at LCLS (1.8×10^{19} W cm^2) [5]. This protein contained two [4Fe–4S] clusters that displayed effects of element specific ionization rates that are a signature of local damage. Hence, the effect of damage on this sample cannot be corrected with global correction factors. Of even greater interest was the observation that the electron density of the two [4Fe–4S] clusters was different in the XFEL dataset but not in the synchrotron dataset. This is evidence that local structure and bonding can impact ionization rate or the distribution of local electron density in XFEL experiments. In the same XFEL experiment, it was unexpectedly observed that the ionization of Fe did not change significantly above and below an ionization edge, which was not expected from simulation. Identifying the physical explanations for the many observations of the ferrodoxin experiment is an outstanding challenge that motivates deeper research into the complex dynamics that can be induced by intense femtosecond X-ray pulses.

It should be noted that femtosecond timescales are sufficient for extensive electron motion or rearrangement. When single crystal xenon clusters are pumped into a plasma state with a femtosecond X-ray pulse, the lattice spacing has been observed to contract on sub-100 fs timescales [9]. Another example is the remarkable observation that the apparent crystalline C_{60} at the maximum available beam intensity at LCLS is different from the known fcc structure that is observed with lower beam intensities and with synchrotron sources [8]. The high-intensity data was shown to agree with a model in which bound electrons rearrange cooperatively across many unit cells to produce a density with lower translational symmetry. Ion motion is a less likely explanation due to the insufficient time for nuclear rearrangement. While such large-scale cooperative effects have not yet been observed in protein crystals, the xenon cluster and C_{60} observations are a reminder that nothing can be taken for granted with extreme intensities produced by X-ray free-electron lasers.

6.6 Damage and Diffraction of Single Molecules

A long-standing goal of XFEL research is to determine structures of single molecules and avoid the need for crystallization [29]. Single molecule diffraction is continuous and much weaker than crystal diffraction, producing as few as a thousand photons per pattern. Nevertheless, it is predicted by imaging analysis theory that sub-3 Å resolution could be achieved with the pulse intensities currently available assuming ideal damage-free, background-free data of reproducible single protein molecules [49]. This has provided motivation for XFEL single molecule imaging to be pursued by large collaborations, most notably the single particle imaging initiative [50]. Currently the best 3D images are of viruses at around ten nanometres resolution. Recovered images have shown the expected size and shape of virus particles at these resolutions [51], which suggests that damage is not significant at these length scales.

XFEL damage to single molecules has been studied with both molecular dynamics [29, 32, 37] and rate equations theory [30]. Theory suggests that there is a self-gating effect in single molecules for global damage processes [52], in the sense that the continuous diffraction retains a strong similarity to the diffraction of the undamaged molecule despite the extra background and noise generated by damage. However, a significant complication is the Coulomb explosion, which can be viewed as a local damage process that has a greater affect on the surface of the molecule [29, 30]. It has been predicted that the trapped electron redistributes to neutralize the core of the positively charged particle, exposing a positively charged shell on the surface of the particle, so that the explosion proceeds layer by layer [30]. The Coulomb explosion is seen as a critical limitation because imaging analysis algorithms that require a rigid structure or have limitations on their ability to handle heterogeneity. One proposal for mitigating the effect of the Coulomb explosion is to use pulses less than 10 fs to outrun the nuclear motion [53]. Another proposal is to use a tamper layer of water around the molecule [54, 55], although the water will generate a background scattering signal that may be problematic for small molecules like proteins.

Even with short pulses to outrun nuclear motion, electronic damage will occur and modify single molecule diffraction. This can viewed as a loss of coherence using the approaches described in Sect. 6.4.5. Encouragingly, a fully coherent model of the diffraction is predicted to adequately account electronic effects of photoionization [42] and secondary ionization [56] in single protein molecules, but would exhibit a modified electron density that differs from the average ion scattering factor. Knowledge of ionization rates would be needed as part of the imaging analysis to correct this effect or at stronger beam intensities where the fully coherent approximation breaks down. There has been some initial work on extending these ideas to the Coulomb explosion and sample heterogeneity [7].

Ultimately the issue of damage in single molecules will not be resolved until higher resolution data is available to test damage theory and to explore the impact of damage on imaging analysis. It remains an outstanding challenge for single molecule imaging development that will become increasingly prominent as single molecule imaging techniques improve in resolution.

6.7 Conclusion

It is a positive outcome for SFX that there are XFEL beam conditions for which conventional crystallography analysis can be applied, and the majority of experiments aimed at structure determination have exploited this knowledge so far.

It is also a positive result that there are sufficient anomalous signals to perform de novo phasing. The developments in understanding global damage corrections point the way to improve conventional crystallographic analysis for XFEL sources.

It has become clear that there are limits on the conditions when local damage can be ignored, which have been exceeded by current sources at their highest beam intensities. These local effects are concentrated on heavier elements that are often biologically important or are used for de novo phasing methods. We expect that the recent availability of two pulse modes at XFELs for X-ray pump-probe experiments will enable future experiments to probe local damage processes and more exotic damage processes observed in xenon clusters and C_{60} crystals in greater detail.

Finally, we note that damage will play an increasingly significant role in extensions of SFX to new phasing methods. Specific mention can be made of direct phasing methods that attempt to exploit scattering between the Bragg peaks or phasing of imperfect crystals that contain structural information in the diffuse continuous scattering. In both these cases, the effect of damage on the diffuse scattering plays a much bigger role that in standard SFX, and will drive the need for better understanding of XFEL damage processes.

References

1. Chapman, H. N., Fromme, P., Barty, A., White, T. A., Kirian, R. A., Aquila, A., et al. (2011). Femtosecond X-ray protein nanocrystallography. *Nature, 470*, 73–77.
2. Boutet, S., Lomb, L., Williams, G. J., Barends, T. R. M., Aquila, A., Doak, R. B., et al. (2012). High-resolution protein structure determination by serial femtosecond crystallography. *Science, 337*, 362–364.
3. Barty, A., Caleman, C., Aquila, A., Timneanu, N., Lomb, L., White, T. A., et al. (2012). Self-terminating diffraction gates femtosecond X-ray nanocrystallography measurements. *Nature Photonics, 6*, 35–40.
4. Galli, L., Son, S.-K., Klinge, M., Bajt, S., Barty, A., Bean, R., et al. (2015). Electronic damage in S atoms in a native protein crystal induced by an intense X-ray free-electron laser pulse. *Structure & Dynamics, 2*, 041703.
5. Nass, K., Foucar, L., Barends, T. R. M., Hartmann, E., Botha, S., Shoeman, R. L., et al. (2015). Indications of radiation damage in ferredoxin microcrystals using high-intensity X-FEL beams. *Journal of Synchrotron Radiation, 22*, 225–238.
6. Son, S.-K., Chapman, H. N., & Santra, R. (2011). Multiwavelength anomalous diffraction at high X-ray intensity. *Physical Review Letters, 107*, 218102.
7. Martin, A. V., & Quiney, H. M. (2016). Coherence loss by sample dynamics and heterogeneity in X-ray laser diffraction. *Journal of Physics B: Atomic, Molecular and Optical Physics, 49*, 244001.
8. Abbey, B., Dilanian, R. A., Darmanin, C., Ryan, R. A., Putkunz, C. T., Martin, A. V., et al. (2016). X-ray laser-induced electron dynamics observed by femtosecond diffraction from nanocrystals of buckminsterfullerene. *Science Advances, 2*, e1601186.
9. Ferguson, K. R., Bucher, M., Gorkhover, T., Boutet, S., Fukuzawa, H., Koglin, J. E., et al. (2016). Transient lattice contraction in the solid-to-plasma transition. *Science Advances, 2*(1), e1500837.

10. Owen, R. L., Rudiño-Piñera, E., & Garman, E. F. (2006). Experimental determination of the radiation dose limit for cryocooled protein crystals. *Proceedings of the National Academy of Sciences of the United States of America, 103*, 4912–4917.
11. Chapman, H. N., Caleman, C., & Timneanu, N. (2014). Diffraction before destruction. *Philosophical Transactions of the Royal Society of London. Series B, Biological Sciences, 369*, 20130313.
12. Auger, P., Ehrenfest, R., Maze, R., Daudin, J. & Fréon, R. A. (1939). Extensive Cosmic-Ray showers. *Reviews of Modern Physics, 11*, 288–291.
13. X-ray data booklet. revision. Technical report, 1986.
14. Hubbell, J. H., Veigele, W. J., Briggs, E. A., Brown, R. T., Cromer, D. T., & Howerton, R. J. (1975). Atomic form factors, incoherent scattering functions, and photon scattering cross sections. *Journal of Physical and Chemical Reference Data, 4*, 471–538.
15. Krause, M. O., & Oliver, J. H. (1979). Natural widths of atomic K and L levels, Kα X-ray lines and several KLL auger lines. *Journal of Physical and Chemical Reference Data, 8*, 329–338.
16. Siegbahn, K. (1970). *ESCA applied to free molecules*. Amsterdam: North-Holland.
17. Persson, P., Lunell, S., Szöke, A., Ziaja, B., & Hajdu, J. (2001). Shake-up and shake-off excitations with associated electron losses in X-ray studies of proteins. *Protein Science, 10*, 2480–2484.
18. Caleman, C. (2007). *Towards Single Molecule Imaging - Understanding Structural Transitions Using Ultrafast X-Ray Sources and Computer Simulations*. Digital Comprehensive Summaries of Uppsala Dissertations from the Faculty of Science and Technology.
19. Ziaja, B., London, R. A., & Hajdu, J. (2005). Unified model of secondary electron cascades in diamond. *Journal of Applied Physics, 97*, 064905.
20. Landau, L. D., & Lifshitz, E. M. (1981). *Quantum mechanics: Non-relativistic theory*. Amsterdam: Elsevier.
21. Caleman, C., Ortiz, C., Marklund, E., Bultmark, F., Gabrysch, M., Parak, F. G., et al. (2009). Radiation damage in biological material: Electronic properties and electron impact ionization in urea. *Europhysics Letters, 85*, 18005.
22. Caleman, C., Huldt, G., Maia, F. R. N. C., Ortiz, C., Parak, F. G., Hajdu, J., et al. (2011). On the feasibility of nanocrystal imaging using intense and ultrashort X-ray pulses. *ACS Nano, 5*, 139–146.
23. Young, L., Kanter, E. P., Krässig, B., Li, Y., March, A. M., Pratt, S. T., et al. (2010). Femtosecond electronic response of atoms to ultra-intense X-rays. *Nature, 466*, 56–61.
24. Caleman, C., Bergh, M., Scott, H. A., Spence, J. C. H., Chapman, H. N., & Tîmneanu, N. (2011). Simulations of radiation damage in biomolecular nanocrystals induced by femtosecond X-ray pulses. *Journal of Modern Optics, 58*, 1486–1497.
25. Caleman, C., Tîmneanu, N., Martin, A. V., Jönsson, H. O., Aquila, A., Barty, A., et al. (2015). Ultrafast self-gating Bragg diffraction of exploding nanocrystals in an X-ray laser. *Optics Express, 23*, 1213–1231.
26. Scott, H. A. (2001). Cretin—A radiative transfer capability for laboratory plasmas. *Journal of Quantitative Spectroscopy and Radiation Transfer, 71*, 689–701.
27. Book, D. L., & Naval Research Laboratory (U.S.). (1987). *NRL plasma formulary*.
28. Gericke, D. O., Murillo, M. S., & Schlanges, M. (2002). Dense plasma temperature equilibration in the binary collision approximation. *Physical Review E, 65*, 036418.
29. Neutze, R., Wouts, R., van der Spoel, D., Weckert, E., & Hajdu, J. (2000). Potential for biomolecular imaging with femtosecond X-ray pulses. *Nature, 406*, 752–757.
30. Hau-Riege, S. P., London, R. A., & Szoke, A. (2004). Dynamics of biological molecules irradiated by short X-ray pulses. *Physical Review. E, Statistical, Nonlinear, and Soft Matter Physics, 69*, 051906.
31. Bergh, M., Tîmneanu, N., & van der Spoel, D. (2004). Model for the dynamics of a water cluster in an X-ray free electron laser beam. *Physical Review. E, Statistical, Nonlinear, and Soft Matter Physics, 70*, 051904.

32. Jurek, Z., Oszlányi, G., & Faigel, G. (2004). Imaging atom clusters by hard X-ray free-electron lasers. *Europhysics Letters, 65*, 491–497.
33. Krejcik, P., Decker, F.-J., Emma, P., Hacker, K., Hendrickson, L., O'Connell, C. L., et al. (2003). Commissioning of the SPPS linac bunch compressor. In: *Proceedings of the 2003 particle accelerator conference*.
34. Lindenberg, A. M., Larsson, J., Sokolowski-Tinten, K., Gaffney, K. J., Blome, C., Synnergren, O., et al. (2005). Atomic-scale visualization of inertial dynamics. *Science, 308*(5720), 392–395.
35. Graziani, F. R., Batista, V. S., Benedict, L. X., Castor, J. I., Chen, H., Chen, S. N., et al. (2012). Large-scale molecular dynamics simulations of dense plasmas: The Cimarron Project. *High Energy Density Physics, 8*, 105–131.
36. Hau-Riege, S. P., & Bennion, B. J. (2015). Reproducible radiation-damage processes in proteins irradiated by intense X-ray pulses. *Physical Review E, 91*, 022705.
37. Jurek, Z., Son, S.-K., Ziaja, B., & Santra, R. (2016). XMDYN and XATOM: Versatile simulation tools for quantitative modeling of X-ray free-electron laser induced dynamics of matter. *Journal of Applied Crystallography, 49*, 1048–1056.
38. Son, S.-K., Young, L., & Santra, R. (2011). Impact of hollow-atom formation on coherent X-ray scattering at high intensity. *Physical Review A, 83*, 033402.
39. Jönsson, H. O., Tîmneanu, N., Östlin, C., Scott, H. A., & Caleman, C. (2015). Simulations of radiation damage as a function of the temporal pulse profile in femtosecond X-ray protein crystallography. *Journal of Synchrotron Radiation, 22*, 256–266.
40. Waasmaier, D., & Kirfel, A. (1995). New analytical scattering-factor functions for free atoms and ions. *Acta Crystallographica. Section A, 51*, 416–431.
41. Slater, J. C. (1930). Atomic shielding constants. *Physical Review, 36*, 57–64.
42. Quiney, H. M., & Nugent, K. A. (2011). Biomolecular imaging and electronic damage using X-ray free-electron lasers. *Nature Physics, 7*, 142–146.
43. Lomb, L., Barends, T. R. M., Kassemeyer, S., Aquila, A., Epp, S. W., Erk, B., et al. (2011). Radiation damage in protein serial femtosecond crystallography using an X-ray free-electron laser. *Physical Review B: Condensed Matter and Materials Physics, 84*, 214111.
44. Barends, T. R. M., Foucar, L., Botha, S., Doak, R. B., Shoeman, R. L., Nass, K., et al. (2014). De novo protein crystal structure determination from X-ray free-electron laser data. *Nature, 505*, 244–247.
45. Galli, L., Barends, T. R. M., Son, S.-K., White, T. A., Barty, A., Botha, S., et al. (2015). Crystal structure of gadolinium derivative of HEWL solved using Free-Electron laser radiation. *IUCrJ, 2*, 627–634.
46. Nakane, T., Song, C., Suzuki, M., Nango, E., Kobayashi, J., Masuda, T., et al. Native sulfur/chlorine SAD phasing for serial femtosecond crystallography. *Acta Crystallographica. Section D, Biological Crystallography, 71*, 2519–2525 (2015)
47. Nass, K., Meinhart, A., Barends, T. R. M., Foucar, L., Gorel, A., Aquila, A., et al. (2016). Protein structure determination by single-wavelength anomalous diffraction phasing of X-ray free-electron laser data. *IUCrJ, 3*, 180–191.
48. Hunter, M. S., Yoon, C. H., DeMirci, H., Sierra, R. G., Dao, E. H., Ahmadi, R., et al. (2016). Selenium single-wavelength anomalous diffraction de novo phasing using an X-ray-free electron laser. *Nature Communications, 7*, 13388.
49. Bortel, G., Faigel, G., & Tegze, M. (2009). Classification and averaging of random orientation single macromolecular diffraction patterns at atomic resolution. *Journal of Structural Biology, 166*, 226–233.
50. Aquila, A., Barty, A., Bostedt, C., Boutet, S., Carini, G., dePonte, D., et al. (2015). The linac coherent light source single particle imaging road map. *Structural Dynamics, 2*(4), 041701.
51. Ekeberg, T., Svenda, M., Abergel, C., Maia, F. R. N. C., Seltzer, V., Claverie, J.-M., et al. (2015, March). Three-dimensional reconstruction of the giant mimivirus particle with an X-ray free-electron laser. *Physical Review Letters, 114*, 098102.

52. Martin, A. V., Corso, J. K., Caleman, C., Timneanu, N., & Quiney, H. M. (2015). Single-molecule imaging with longer X-ray laser pulses. *IUCrJ, 2*, 661–674.
53. Hau-Riege, S., London, R., Huldt, G., & Chapman, H. (2005). Pulse requirements for X-ray diffraction imaging of single biological molecules. *Physical Review E, 71*, 061919.
54. Hau-Riege, S. P., London, R. A., Chapman, H. N., Szoke, A., & Timneanu, N. (2007). Encapsulation and diffraction-pattern-correction methods to reduce the effect of damage in X-ray diffraction imaging of single biological molecules. *Physical Review Letters, 98*, 198302.
55. Hau-Riege, S. P., Boutet, S., Barty, A., Bajt, S., Bogan, M. J., Frank, M., et al. (2010). Sacrificial tamper slows down sample explosion in flash diffraction experiments. *Physical Review Letters, 104*, 064801.
56. Lorenz, U., Kabachnik, N. M., Weckert, E.., & Vartanyants, I. A. (2012). Impact of ultrafast electronic damage in single-particle X-ray imaging experiments. *Physical Review B, 86*, 051911.